Surface & Coatings Technology 456 (2023) 129262

Contents lists available at ScienceDirect

Surface & Coatings Technology

journal homepage: www.elsevier.com/locate/surfcoat

The influence of laser shock peening on corrosion-fatigue behaviour of wire arc additively manufactured components

Anna Ermakova [a], Jarryd Braithwaite [b], Javad Razavi [c], Supriyo Ganguly [d], Filippo Berto [c], Ali Mehmanparast [a,*]

[a] Department of Naval Architecture, Ocean and Marine Engineering, University of Strathclyde, Glasgow G1 1XQ, United Kingdom
[b] School of Aerospace, Transport and Manufacturing, Cranfield University, Cranfield MK43 0AL, United Kingdom
[c] Norwegian University of Science and Technology (NTNU), Trondheim, Norway
[d] Welding Engineering and Laser Processing Centre, Cranfield University, Cranfield MK43 0AL, United Kingdom

ARTICLE INFO

Keywords:
Wire arc additive manufacturing
Corrosion-fatigue
Surface treatment
Laser shock peening
Residual stress

ABSTRACT

The need for increased manufacturing efficiency of large engineering structures has led to development of wire arc additive manufacturing (WAAM), which is also known as direct energy deposition (DED) method. One of the main barriers for rapid adoption of the WAAM technology in wider range of industrial applications is the lack of sufficient performance data on the WAAM components for various materials and operational conditions. The present study addresses this essential need by exploring the effects of laser shock peening surface treatment on corrosion-fatigue crack growth (CFCG) life enhancement of WAAM components made of ER70S-6 and ER100S-1 steel wires. The experimental results obtained from this study were compared with the CFCG trends from nominally identical specimens without surface treatment and prove the efficiency of the examined surface treatment method for corrosion-fatigue life enhancement and crack growth retardation of WAAM built steel components, regardless of the material type and specimen orientation. Furthermore, the residual stresses in the WAAM built specimens with and without surface treatment were measured to validate the influence of beneficial residual stresses, arising from surface treatment, on subsequent CFCG behaviour of the material. The residual stress profiles show the beneficial compressive stress fields in the surface treated areas which result in CFCG life enhancement. The results from this study make significant contribution to knowledge by evaluating the suitability of WAAM built steel components for application in offshore environments.

1. Introduction

Nearly all engineering structures experience some form of cyclic loading condition during their lifetime, which results in fatigue damage. The fatigue performance of engineering structures can be significantly deteriorated in the presence of harsh environmental conditions. For example, the offshore structures in oil and gas, and renewable energy industries are subjected to cyclic loads caused by wind, waves, and current, while they operate in the highly corrosive marine environment [1]. A combination of these factors may lead to premature failure of the structures during their operation, making corrosion-fatigue the main mode of failure for offshore structures. Thus, it is essential to develop new high strength materials and manufacturing techniques to enhance the corrosion-fatigue resistance of offshore structures to extend their operational lifespan. A number of life enhancement techniques have been developed and implemented by various industries in the past, including mechanical and surface treatment methods, to improve the fatigue performance of engineering structures. Grinding is a widely used mechanical technique [2], designed particularly for the weld toes, to reduce high stress concentrations and subsequently increase the fatigue life of the welded component. Moreover, several surface treatment techniques can be used to induce compressive residual stress fields at the outer surface of the component and slow down the crack initiation and propagation processes. A number of surface treatment methods have already been actively implemented in a wide range of engineering applications such as surface rolling [3–7], shot peening [8–12], laser shock peening [13–15] and vibro peening [16]. They differ by the complexity of the treatment process, cost, penetration depth and hence the efficiency, which will also depend on the material properties and industrial application.

Wire arc additive manufacturing (WAAM), which is a type of direct

* Corresponding author.
E-mail address: ali.mehmanparast@strath.ac.uk (A. Mehmanparast).

https://doi.org/10.1016/j.surfcoat.2023.129262
Received 27 October 2022; Received in revised form 9 January 2023; Accepted 14 January 2023
Available online 21 January 2023

Nomenclature

a_0	initial crack length in C(T) specimen
a_i	instantaneous crack length
$a_{i,p}$	initial crack length in C(T) specimen after pre-cracking
$a_{f,c}$	estimated final crack length at the end of the test
Δa	crack extension
B	total thickness of C(T) specimen
C	material constant
d_0	stress-free reference value for lattice spacing
d	lattice spacing
da/dN	CFCG rate
E	Young's modulus
H	height of C(T) specimen
hkl	Miller indices
J	the power density in laser shock peening process
K	stress intensity factor
K_{eff}	effective stress intensity factor
K_{max}	maximum stress intensity factor
K_{RS}	residual stress intensity factor
m	material constant
N	number of cycles
P_{max}	maximum load in a fatigue cycle
P_{min}	minimum load in a fatigue cycle
R	load ratio
W	width of C(T) specimen
ε	residual strain
η	geometry dependent function
θ	scattering angle
λ	wavelength
ν	Poisson's ratio
σ_i	stress component
σ_Y	yield stress
AM	additive manufacturing
C(T)	compact tension specimen geometry
CMT	Cold Metal Transfer
COD	Crack Opening Displacement
DED	Directed Energy Deposition
EDM	Electrical Discharge Machining
FCG	Fatigue Crack Growth
H	horizontal specimen orientation
LP	laser shock peening surface treatment
MUD	multiple of uniform density
SIF	stress intensity factor
V	vertical specimen orientation
WAAM	Wire Arc Additive Manufacturing

energy deposition (DED) additive manufacturing (AM) technology, is a fabrication process to 3D print large scale metallic parts or repair the damaged components. Compared to conventional manufacturing methods for metals and other DED techniques, WAAM is an advantageous and cost-effective method for fabrication of large scale structures, which can improve the mechanical properties, and enable hybrid manufacturing by involving combination of materials [17,18]. However, on the other hand it presents some challenges, such as complex residual stress profiles and surface roughness, which directly affect the fatigue performance of the WAAM built parts [19–22]. The tensile residual stresses have damaging effect on structural integrity by accelerating the crack initiation and propagation. Therefore, material treatments are often required during deposition process or post-manufacturing to enhance the integrity of WAAM built components. The most common material treatment method that has been examined in the past for life enhancement of WAAM built parts is inter-pass rolling that is usually applied on top of each deposited AM layer, while building the part. Several research groups reported the effectiveness of this method, and its ability to lengthen the fatigue life of WAAM parts made of titanium [23,24], aluminum [25], steel [26] and stainless steel [27]. While inter-pass rolling has proved to enhance the fatigue behaviour of the WAAM built components, it considerably increases the manufacturing time, effort, and cost. Hence, there is need to examine alternative material treatment techniques, particularly post-manufacturing surface treatment processes, to enhance the fatigue response of WAAM built components in much shorter time scales.

Among all surface treatment techniques laser shock peening, which is also known as laser peening (LP), offers a greater penetration depth, hence higher values of induced compressive residual stresses that subsequently result in higher fatigue resistance in the treated areas [8,13]. This is why LP is usually used for the critical mechanical components, which contain notches, holes, or sharp corners prone to fatigue failure. As reflected in the recent studies, this surface treatment method has great potential to address the main challenges involved in integrity management of WAAM components made of various metallic materials [28]. Laser peening, used as a post-processing method on WAAM built aluminum specimens by Sun et al. [29], showed microstructural refinement and increase in micro-hardness of the examined material, as well as transformation of tensile stresses into compressive stresses, resulting in 72 % yield strength improvement. Comparable conclusions were drawn by Luo [30] and Chi [31], on tested WAAM specimens made of titanium, confirming the benefits of LP surface treatment technique [32]. Also, a study by Wang et al. [33] is available on LP treated wrought aluminum specimens, which presented promising results with an increase of corrosion-fatigue life by 29.3 % using gradient laser pulse energies. The existing test data available in the literature are mainly focused on aerospace applications, hence why the past research attempts have been conducted on materials such as titanium and aluminum. However, no data is available on life enhancement options for WAAM built steels particularly for industrial applications where the structure is subjected to corrosion-fatigue loading conditions such as offshore structures. The above findings highlight the need for a systematic investigation of the effectiveness of the LP surface treatment technique for corrosion-fatigue life enhancement of WAAM built steel structures to expand the application of the WAAM technology to offshore environments.

In order to fill in the research gap, this study investigates the influence of LP surface treatment technique on corrosion-fatigue crack growth (CFCG) behaviour of WAAM built specimens made with different grades of steel, namely ER70S-6 and ER100S-1. The results obtained from this study are compared with the CFCG performance of nominally identical untreated WAAM specimens to quantify the extent of life enhancement in the presence of LP treatment. Furthermore, the results from CFCG tests were interpreted by measuring the residual stresses in untreated and treated specimens, revealing the cause of the beneficial impact of LP on CFCG behaviour of WAAM specimens.

2. Specimen fabrication and preparation

2.1. Manufacturing procedure

For the current study, two WAAM walls were fabricated, one using the ER70S-6 and one using ER100S-1 steel wires. Four specimens were extracted in total; two from the WAAM wall fabricated using ER70S-6 mild steel [34], and two from WAAM wall made of ER100S-1 steel wire [35]. The chemical composition of both materials employed in this study is presented in Table 1. Both WAAM walls were manufactured by the Cold Metal Transfer (CMT) process, using parameters summarised in

Table 1
Chemical composition of the steel wires (wt.-%) [34,35].

	C	Mn	Cr	Si	Ni	Mo	S	P	Cu	V
ER70S-6	0.09	<1.60	0.05	0.09	0.05	0.05	0.007	0.007	0.20	0.05
ER100S-1	0.08	1.70	0.20	0.60	1.50	0.50	–	–	–	–

Table 2
WAAM-CMT system fabrication parameters.

Shielding gas	Ar + 20 % CO_2
Gas flow rate	15 L/min
Robot travelling speed	7.33 mm/s
Wire diameter	1.2 mm
Wire feed speed	7.5 m/min
Dwell time	120 s

Table 2. The WAAM-CMT system set-up is shown in Fig. 1, which typically consists of the CMT power source, that feeds the welding wire at a set speed. During this process, the wire is fed through a pre-programmed robotic arm, which also supplies shielding gas, and the electric arc melts the wire and deposits the material onto the base plate with the torch. The base plate was rigidly attached to the working table with clamps that prevented the plate and wall from distortion and bending due to extreme manufacturing temperatures. Once the deposited WAAM wall was cooled to ambient temperature, the clamps were released. Due to the large thickness of the designed WAAM walls, the oscillation deposition strategy [36] was employed to achieve the thickness of 24 mm (Y-axis in Fig. 1), with approximate length of 355 mm (X-axis), and height of 140 mm (*Z*-axis).

Two compact tension, C(T), specimens were extracted from each WAAM wall using the Electrical Discharge Machining (EDM) method, in vertical (V) and horizontal (H) orientations. Specimens extracted from ER70S-6 wall were denoted as '70', and those from ER100S-1 wall denoted as '100'. As shown in Fig. 1, in vertical specimen the crack plane is perpendicular to the deposited additive layers, whereas in horizonal specimen it is parallel to the deposited layers. The C(T) specimens were designed according to ASTM E647 standard [37], with the width of $W = 50$ mm, height of $H = 60$ mm, thickness of $B = 16$ mm and the initial crack length before pre-cracking of $a_0 = 17$ mm. Also, according to the ASTM 1820 standard [38] knife edges were designed at the crack mouth of the specimens, in order to accommodate a Crack Opening Displacement (COD) gauge for crack growth monitoring during pre-cracking stage, which is required prior to CFCG tests.

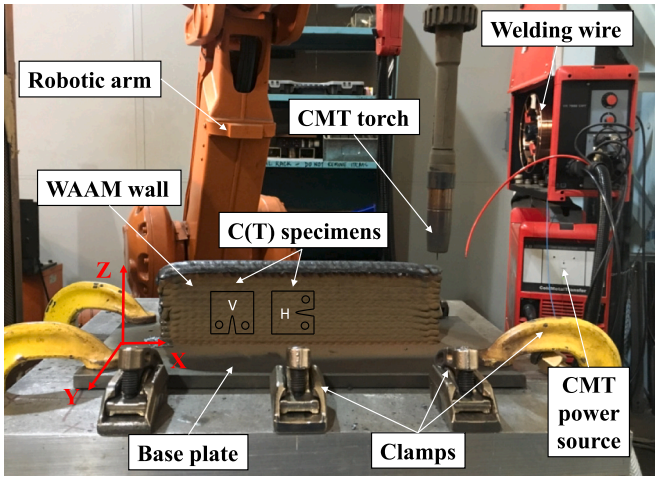

Fig. 1. WAAM-CMT system set-up with schematic display of specimen orientations.

2.2. Surface treatment on WAAM built specimens

After extraction of the specimens from the WAAM walls, they were subjected to laser shock peening (LP) surface treatment. A small rectangular area with dimensions of 20 × 12 mm^2 was treated on both sides of C(T) specimens as shown in Fig. 2(a) and (b), where the area ahead of the notch tip was 20 × 8 mm^2, following the suggestion made in a study by Pi et al. [39] The following parameters were adopted during the treatment: spot size of 3 mm^2, pulse duration of 18 ns, energy level of 8.1 with the power density of $J = 5$ GW/cm^2, three layers of treatment, providing 300 % coverage (presented in Fig. 2(a)). Following application of LP surface treatment on C(T) specimens, all four specimens were pre-cracked on Instron 100 kN servo hydraulic machine to approximately 20 mm ($a/W = 0.4$) crack length using the load-decreasing approach, ensuring that the final value of maximum stress intensity factor K_{max} at the end of pre-cracking process is not exceeding the initial K_{max} at the beginning of CFCG tests. At the final stage of specimen preparation, strain gauges were attached at the back of the specimens (see Fig. 2(c)) and then covered with protective polysulfide coating as shown in Fig. 2(d), to perform the crack growth measurements in seawater during CFCG tests, which is explained further in the following section.

3. Corrosion-fatigue crack growth testing and analysis procedure

3.1. Test set-up

To replicate the free-corrosion environment for CFCG tests, the artificial seawater was prepared following the guidelines provided in ASTM D1141-98 standard [40] with deionised water and combination of chemicals, presented in Table 3. The pH level of the seawater was monitored to ensure it is maintained between 8.0 and 8.2, and once it dropped below 8.0 it was replaced with freshly prepared seawater. Prior to testing, specimens were soaked in the seawater for at least 24 h, as advised in the standard. The CFCG test set-up is displayed in Fig. 3 [41], which consists of 100 kN servo hydraulic Instron machine, seawater tank that contained 60 L of seawater, water pumps that circulated seawater through the environmental chamber attached onto Instron machine at a constant rate of 4 L/min. The C(T) specimen was positioned in the chamber in such a way that the crack plane was constantly

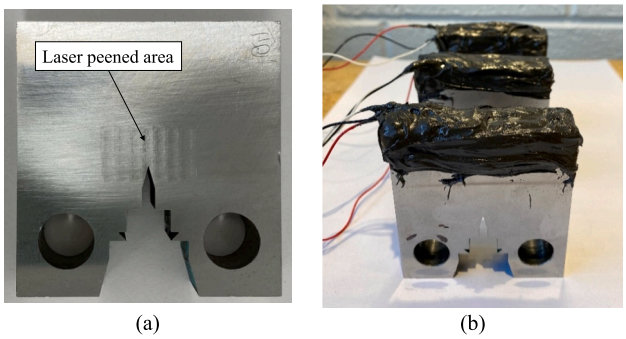

(a) (b)

Fig. 2. C(T) specimen with (a) a patch after third layer of LP application (300 % coverage), (b) after LP treatment process, (c) schematic illustration of BFS location, and (d) protective coating over the strain gauge attached to the back of the sample.

Table 3
The chemical used for preparation of artificial seawater [40].

	NaCl	$MgCl_2$	Na_2SO_4	$CaCl_2$	KCl	$NaHCO_3$	KBr	H_3BO_3	$SrCl_2$	NaF
Concentration (g/L)	24.53	5.20	4.09	1.16	0.695	0.201	1.101	0.027	0.025	0.003

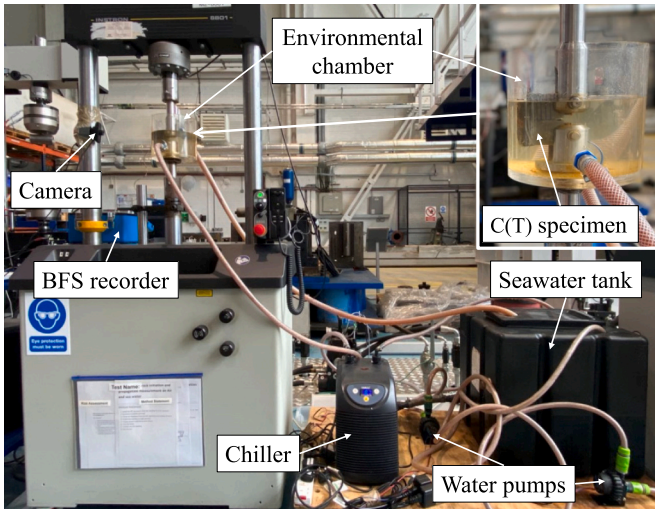

Fig. 3. Corrosion-fatigue crack growth test set-up.

immersed in water throughout the test. A chiller maintained the temperature of the seawater between 8.0 and 10.0 °C to replicate the conditions in the North Sea [1]. A camera was attached to the machine for constant observation and monitoring of the lengthy CFCG test. The CFCG tests were conducted under load-controlled mode, with the maximum load of $P_{max} = 10$ kN, load ratio of $R = 0.1$, and frequency of $f = 0.3$ Hz, which is typically used for corrosion-fatigue assessment of offshore wind turbine structures [42,43]. As shown in Fig. 3, the C(T) specimen was marked prior to immersion in water to highlight the desired crack length of 35 mm ($a_{f,c}/W = 0.7$), which indicated the end of test once the crack grew to length.

3.2. Crack growth monitoring technique

During the CFCG test, the specimen is located underwater limiting the access for visual or mechanical crack monitoring techniques. One of the few known methods for crack estimation applicable for environmental tests is the back face strain (BFS) technique [44,45]. The idea is to correlate the BFS data with the crack length of the specimen. For this purpose, strain gauges are attached to the back of the specimens at the mid-height and mid-thickness, which react to specimen deformation during the test (due to crack growth and hence specimen mouth opening and reduction in stiffness). The data is recorded by a a strain gauge indicator recording device (BFS recorder) that monitors the variation in strain at the back of the specimen throughout the test (shown in Fig. 3). In order to correlate the BFS data recorded during the CFCG test with the crack length, a calibration curve needs to be obtained from the FCG test in air on a nominally identical C(T) specimen. During the FCG calibration test, the BFS data from the strain gauge and the crack length obtained from the COD gauge using the unloading compliance method are recorded simultaneously to plot them against each other and develop empirical correlation for a particular C(T) specimen geometry with a given loading condition.

Therefore, prior to the main CFCG tests, four nominally identical C(T) specimens, with the same design, material, extraction orientations and LP surface treatment were tested in air. Knowing that the BFS calibration curve depends on the loading conditions, the FCG calibration tests were conducted under the exact same loading condition as the CFCG tests, which are summarised in Table 4. Four empirical correlations between BFS data and crack length were developed for WAAM ER70S-6 and ER100S-1, vertical and horizontal specimens.

Furthermore, to verify the accuracy of the crack length estimation obtained with the BFS technique, the beach marking (BM) method [46] was implemented during the tests in air and seawater. This method requires reduction of the maximum applied cyclic load and/or frequency for a short period of time during the test, which leaves a visible thin line on the fracture surface of the specimen, which is also known as beach mark. The duration of BM cycles has to be carefully selected to ensure that the crack does not considerably propagate during the process and hence BFS value remains unchanged. When the BM method is employed, the corresponding value of BFS is recorded. Upon completion of the test, the crack length is measured on the fracture surface of the broken specimen and correlated with corresponding BFS value at particular beach marks. The BM method was first evaluated on the specimens tested for FCG in air. An example of the fracture surface of ER100S-1 specimen with beach marks is shown in Fig. 4. Once the procedure and required outcome were verified, this method was implemented in the CFCG tests, repeating BM three times throughout each test to generate enough data points to cross-check the results from BFS method. Prior to the test, each C(T) specimen was marked on the outer surface to identify the approximate locations for the three pre-planned beach marks (Fig. 3). The BM loading conditions for tests in air and seawater are shown in Table 4.

Upon completion of the CFCG tests, all four C(T) specimens were broken open and their fracture surfaces were analysed, as displayed in Fig. 5. It can be seen in this figure that all specimens were severely corroded during the tests, hence the BM lines were not as visible as the ones on the specimens tested in air (Fig. 4). Thus, optical microscopy was used to identify the exact location of the marks in CFCG specimens. An example of the calibration curve obtained with the BFS method and additional BM data collected for 70-H-LP specimen are shown in Fig. 6, which indicates good agreement and confirms the accuracy of crack estimation methods implemented in this study. Further microstructural analysis was not conducted due to the high level of corrosion on the specimen surface. However, some EBSD assessment has been completed on the nominally identical specimens tested for fatigue crack growth tests in air by Ermakova et al., where it was reported that there is no major effect on both texture index and grain size of the treated specimens [47].

3.3. Data analysis method

Using the estimated crack lengths from the BFS method and the corresponding number of cycles, the CFCG rates, da/dN was computed by applying the secant method for the first three and last three data points, and seven-point incremental polynomial method for the rest of the data points. Subsequently, the stress intensity factor (SIF) was determined using the shape function equation proposed by Mehmanparast et al. [41] and shown in Eq. (1), where $\alpha = a/W$ is the normalised

Table 4
Test loading conditions for air and seawater environments.

Test environment	The main test condition			Beach marking loading condition		
	P_{max} (kN)	R	f (Hz)	P_{max} (kN)	R	f (Hz)
Air	10	0.1	5	8	0.125	3
Seawater	10	0.1	0.3	8	0.125	0.1

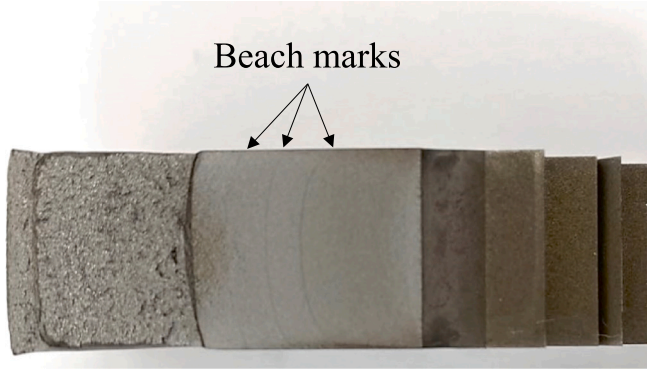

Fig. 4. Visible beach marks on a broken ER100S-1 specimen FCG tested in air.

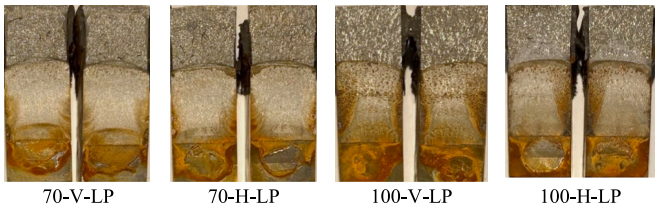

Fig. 5. Fracture surfaces of the CFCG tested WAAM specimens.

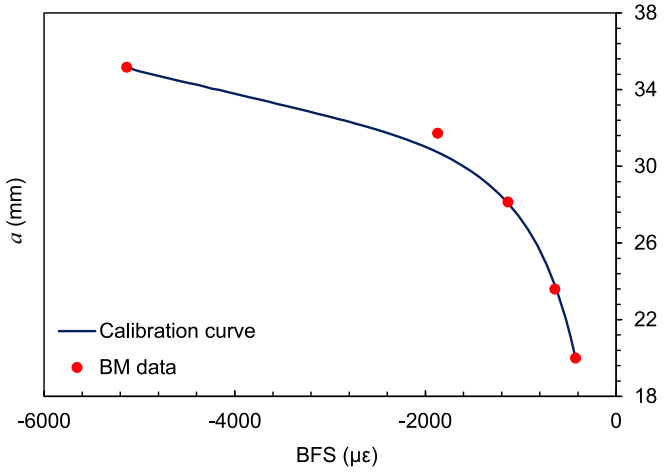

Fig. 6. Comparison of the produced "crack length vs. BFS" calibration curve with the data collected through BM method for 70-H-LP specimen.

crack length and ΔP is the difference between the maximum load P_{max} and the minimum load P_{min}.

$$\Delta K = \frac{\Delta P}{BW}\cdot\sqrt{a}\cdot\left(-372.12\alpha^6 + 1628.60\alpha^5 - 2107.46\alpha^4 + 1304.65\alpha^3 - 391.20\alpha^2 + 54.81\alpha + 7.57\right) \quad (1)$$

4. Results and discussions

The results obtained from this study on LP surface treated specimens were plotted and compared with the results of CFCG tests on nominally identical specimens without surface treatment from previous studies by Ermakova et al. on ER70S-6 [48] and ER100S-1 [49] C(T) specimens. The results were initially evaluated in terms of the test duration by plotting the crack length values, *a*, against number of cycles, *N*, as shown in Fig. 7(a) for ER70S-6 and Fig. 7(b) for ER100S-1 specimens. It can be seen from the figure, that for both materials and orientations the required number of cycles to propagate the crack to 35 mm has increased for LP specimens despite the material type and extraction orientation. Also, it can be noted here that the increase in number of cycles is comparatively smaller for horizontal specimens (2.4 % for 70-H-LP and 19.3 % for 100-H-LP), whereas for vertical specimens the shift is more pronounced (45.8 % for 70-V-LP and 40.5 % for 100-V-LP specimens). The obtained trends indicate that the duration of the test increased mostly while the crack was growing through the treated area of the specimens (treated area after pre-cracking is from 20 mm to approximately 25 mm of the crack length) and once the crack extends outside the surface treatment area the trends for treated and untreated specimens gradually become almost parallel. The dashed grey lines in Fig. 7(a) and (b) divide the crack growth into two regions: the first one affected by the surface treatment at the crack length of between 20 and approximately 28 mm, and the second area without surface treatment, which starts from a crack length of approximately 28 mm. It is expected that this effect is caused by induced compressive stresses from LP surface treatment technique and redistribution of the initial residual stresses in the specimens, which is discussed in Section 5.

The CFCG rates (da/dN) calculated for each LP specimen were plotted against the SIF, ΔK, and compared with the results from untreated specimens in Fig. 8 for (a) ER70S-6 and (b) R100S-1 specimens. It can be observed from the figure that at lower values of ΔK, hence shorter crack lengths, and all four surface treated specimens show improved CFCG rates in comparison with the results for untreated specimens. The best result is presented by 100-V-LP specimen, in which the CFGC rate is lower than untreated specimen throughout the test. It can be seen in Fig. 8 that the CFCG rate in 100-V-LP specimen was almost constant up to 26 mm (which corresponds to the end of the LP treated area ahead of the crack tip), beyond which the CFCG trend started to follow the trend of the untreated specimen, although with cracking rate of on average 30 % lower. Very close trend pattern is also seen for 70-H-LP and its untreated counterpart, where the cracking rates show minor improvement up to 30 mm of crack growth. The trend for 70-V-LP specimen is very steep compared with untreated specimen results, indicating the enhanced crack growth rates for the period of test (up to 26.5 mm) when the crack was growing through the treated area; however, with the increase in the crack length and ΔK values, the corrosion-fatigue resistance was reduced dramatically compared with the corresponding untreated specimen. Similarly, 100-H-LP specimen demonstrated improved CFCG behaviour at the lower values of ΔK (up to 27.6 mm), which is then undertaken by untreated specimen. The above observations lead to a conclusion that despite the material and specimen extraction orientation, corrosion-fatigue life enhancement is achievable by LP surface treatment technique for WAAM fabricated mild steel specimens within the treated area. Furthermore, the effect of LP strongly depends on the size of the treated area, as shown by test duration (Fig. 7) and CFCG rate (Fig. 8) results.

5. Residual stress assessments

In order to have an accurate interpretation of the CFCG results from the surface treated specimens presented in the previous section, the residual stress distribution profiles in ER100-1 vertical specimens (100-V) were examined before and after LP application. Two non-destructive techniques were used in this study: neutron diffraction and X-ray. The neutron diffraction method offers a deeper penetration depth compared with X-ray, which only captures the stresses in the near surface region. Thus, the changes in residual stress state in the middle of the specimen caused by LP treatment were measured using the neutron diffraction method while the X-ray technique was used to depict the residual stresses at the outer surface of the treated specimen.

5.1. Neutron diffraction measurements

The initial residual stresses in the 100-V untreated specimen were measured by SALSA strain diffractometer at the Institut Laue-Langevin

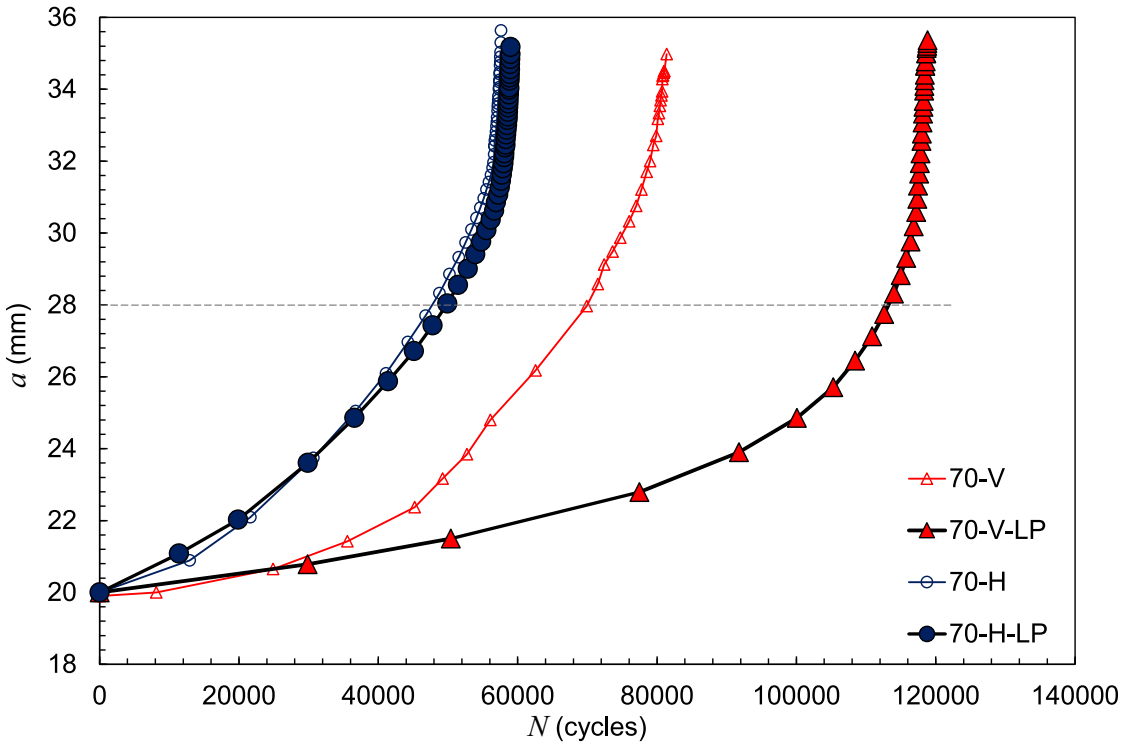

(a)

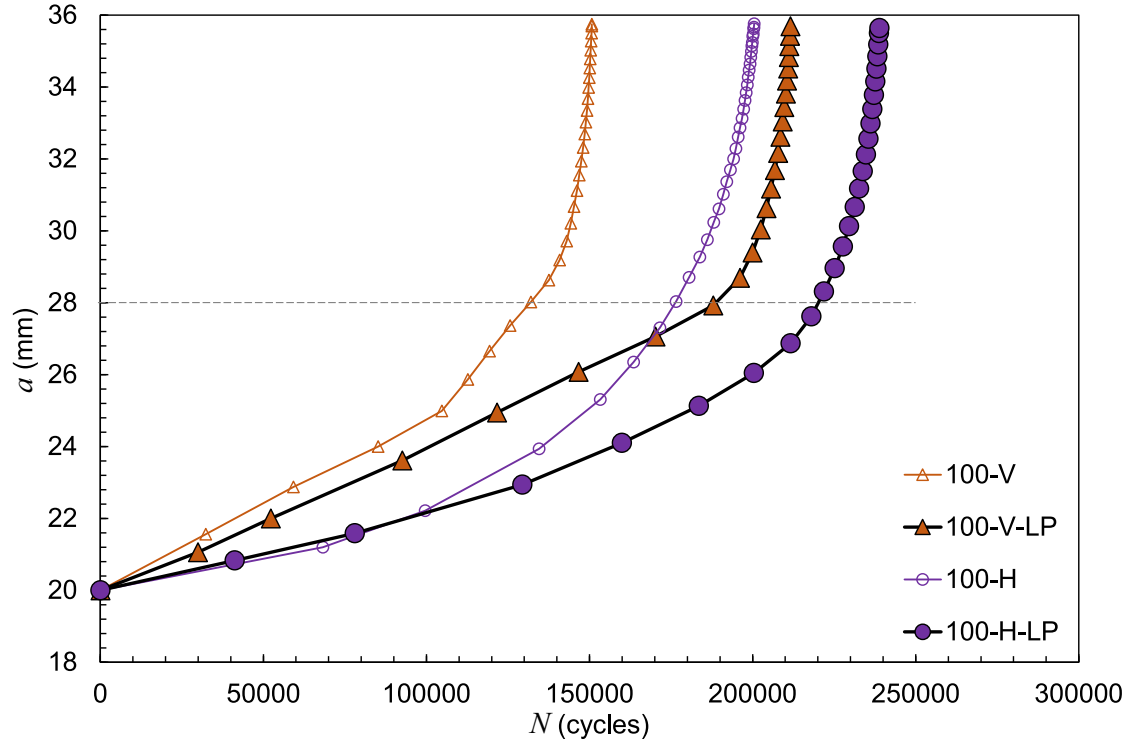

(b)

Fig. 7. Comparison of the crack growth trends from WAAM specimens with and without LP surface treatment for (a) ER70S-6, and (b) ER100S-1 materials.

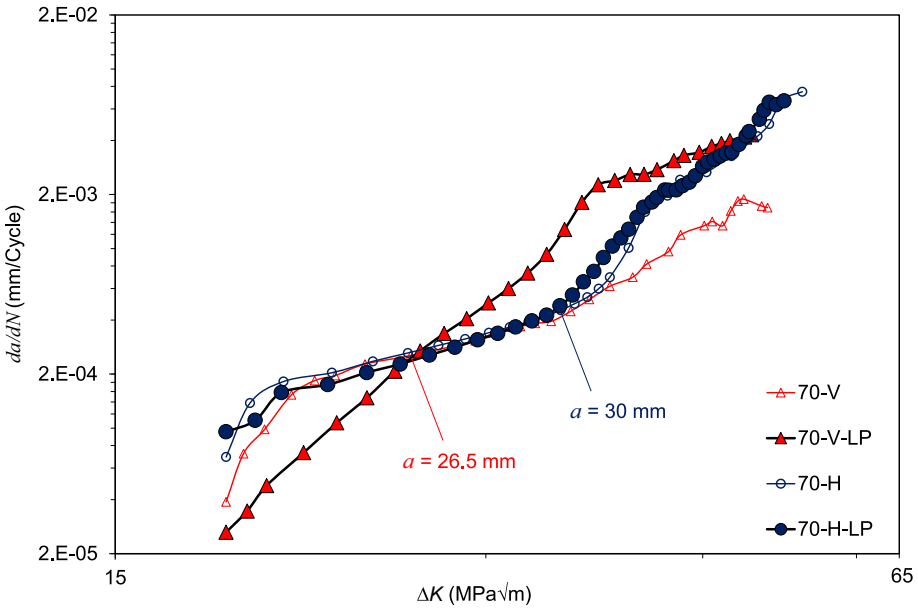

(a)

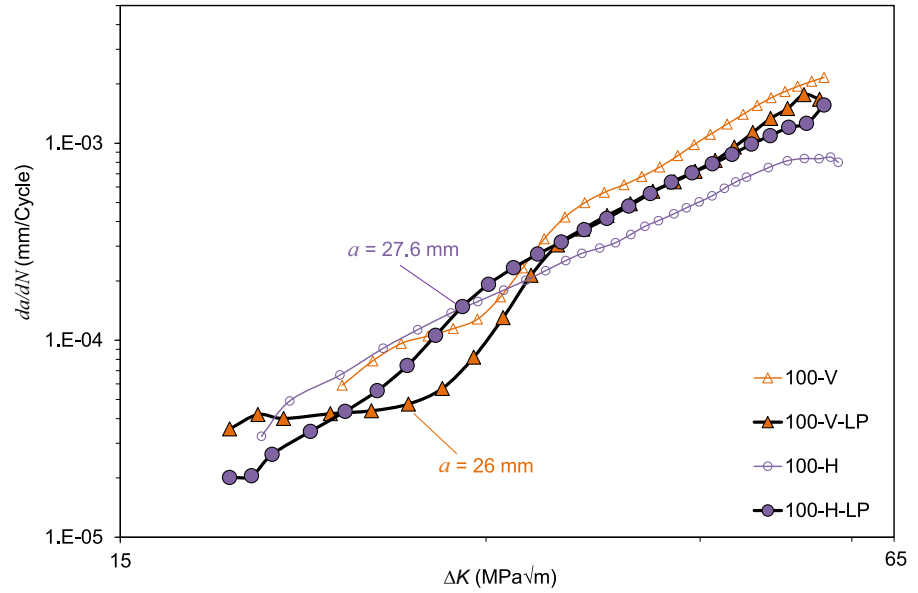

(b)

Fig. 8. Comparison of CFCG rates from WAAM specimens with and without LP surface treatment for (a) ER70S-6, and (b) ER100S-1 materials.

(ILL)-France [50]. After applying the LP surface treatment, the specimen's residual stress profile was measured again using KOWARI strain scanner at the Australia's Nuclear Science and Technology Organisation (ANSTO). A similar set-up was employed in both institutes (see Fig. 9 (a)), where the neutron wavelength was fixed, and the diffraction angle was measured. Subsequently, the lattice spacing parameter d was calculated using Bragg's law [51]:

$$n\lambda = 2d_{hkl}sin\theta_{hkl} \tag{2}$$

where n is a constant, λ is the neutron wavelength, d is the lattice spacing or the distance between sets of parallel crystallographic planes characterised by the Miller indices hkl, and θ is the scattering angle. In the next step, the elastic strain was computed by employing the changes in the lattice spacing (Δd) using the following equation:

$$\varepsilon_{hkl} = \frac{\Delta d_{hkl}}{d_{0,hkl}} = \frac{d_{hkl} - d_{0,hkl}}{d_{0,hkl}} \tag{3}$$

where d_0 is stress-free value of lattice spacing, measured in the cubes with the dimensions of 5 × 5 × 5 mm^3, extracted along the crack path from nominally identical specimens without any surface treatment. The selected approach for d_0 on multiple cube samples, minimises the error in neutron diffraction results by considering the variations in heterogeneous properties of AM specimens.

The residual stress in each direction was then calculated from the residual strains using Hooke's law, which can be described as:

$$\sigma_i = \frac{E}{(1+\nu)(1-2\nu)}\left[(1-\nu)\varepsilon_i + \nu\left(\varepsilon_j + \varepsilon_k\right)\right] \tag{4}$$

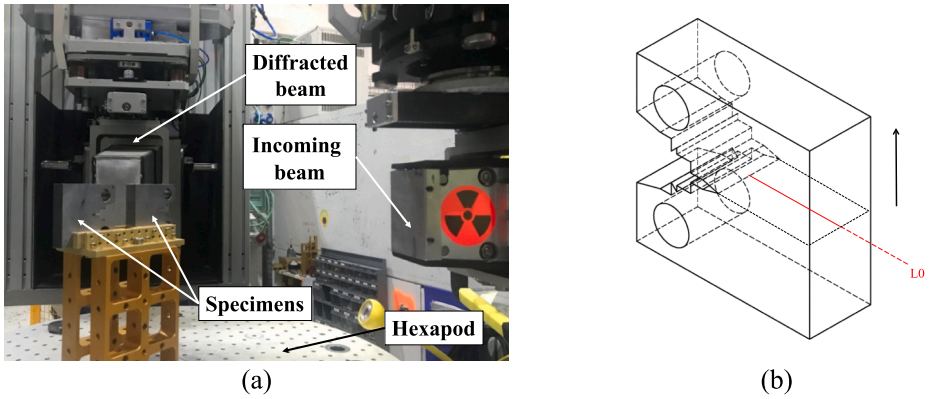

Fig. 9. Neutron diffraction (a) measurement set-up, and (b) measurement line with respect to the specimen thickness (the arrow indicates the residual stress component of interest).

where E is the elastic Young's modulus and ν is Poisson's ratio. The crystallographic values of the elastic modulus and Poisson's ratio used in this study were $E = 210$ GPa and $\nu = 0.25$ [52]. Gauge volume was set to $2 \times 2 \times 2$ mm^3 for the experiments, conducting the measurements in the middle of the specimen along the crack propagation line, depicted as L0 in Fig. 9(b). In this figure, the stress component of interest is shown with black arrow, which is normal to the crack plane.

5.2. X-ray diffraction method

During application of the LP surface technique onto 100-V specimen (100-V-LP), the residual stresses at the outer surface of the specimen were measured using a Malvern Panalytical EMPYREAN diffractometer. The maximum penetration depth of the measurement was 37.5 μm from the outer surface. Similar to the neutron diffraction measurements, surface X-ray (XR) examination was conducted along the crack path, ahead of the crack tip of the specimen, with intervals of 1 mm. The component of stress perpendicular to the crack plane was recorded, which represents the direction of the applied load during the CFCG tests.

5.3. Residual stress distribution trends

The residual stress measurement results obtained on ER100S-1 vertical specimen before and after LP treatment are presented in Fig. 10. It can be seen in this figure that the initial residual stress state at the mid thickness of the specimen (100-V-L0) consists of the tensile stresses up to 407 MPa. However, once the LP was applied (100-V-LP-L0) the residual stresses in the middle of the specimen were reduced dramatically to values between 25 and 86 MPa of tensile stress. As for the residual stresses at the specimen surface measured with X-ray technique (100-V-LP-XR), a clear trend of compressive stresses introduced in the treated area of the specimen can be observed. The maximum amplitude of compressive stress is −134 MPa, and the compressive stress region is up to the crack length of 27 mm, even though the edge of the LP treated zone is at approximately 25 mm. From 27 mm onwards the overall residual stress distribution in the sample is balanced by the tensile stress profile, with the maximum amplitude of 401 MPa, in the region beyond the surface treated area. The observed behaviour of the residual stresses in the specimen caused by the LP application can explain the improved CFCG performance in the LP surface treated region at low values of ΔK, as described in Section 4. It can be concluded that the enhancement of the CFCG behaviour, which was observed for at least the first 8 mm of the crack propagation region (up to 28 mm crack length) in Fig. 7(b) and in almost constant CFCG rates for up to 26 mm of the crack length in Fig. 8(b), is corresponding to the compressive stress region highlighted by the X-ray residual stress measurements in the same region up to 27 mm. Subsequently, the CFCG rates deterioration at larger crack length (Fig. 8(b)) is corresponding to the tensile stress profile region shown by the X-ray measurements (beyond 27 mm crack length). The influence of residual stresses on the CFCG rates can be explained through the effective stress intensity factor, presented in Eq. (5), where K_{ap} is the applied SIF during CFCG tests, and K_{RS} is the residual stress SIF [53].

$$K_{eff} = K_{ap} + K_{RS} \tag{5}$$

It is evident from this equation that the compressive residual stresses,

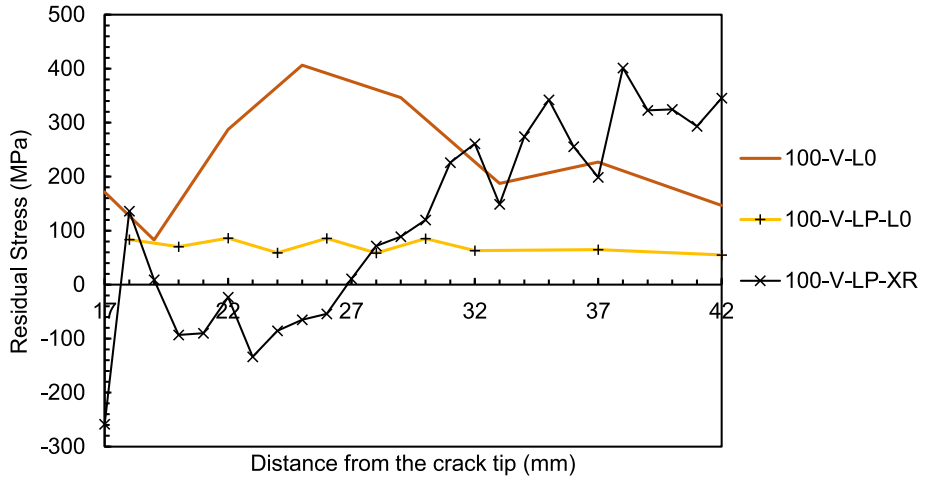

Fig. 10. Residual stress distribution in 100-V specimen before and after surface treatment.

located near the crack tip region, reduce the value of the effective SIF, which simultaneously leads to an exponential reduction in the CFCG rates, as seen in Eq. (6), where C and m are material constants. Conversely, the tensile residual stresses could increase the CFCG rates as a result of increase in the effective SIF value.

$$da/dN = C\Delta K^m \quad (6)$$

6. Conclusions

In the current study the effectiveness of surface treatment techniques on CFCG life enhancement of ER70S-6 and ER100S-1 WAAM built C(T) specimens were examined by applying laser shock peening at the area near the crack tip. The CFCG tests were performed on specimens with laser shock peening treatment and the results were compared with those without any surface treatment. The following results and observations could be made from this study:

- Laser shock peening was found to be an efficient method for deceleration of CFCG rates and improvement of lifespan in WAAM built specimens made of two different steel wires examined in this study.
- The laser shock peening surface treatment improved the CFCG performance despite the specimen orientation with respect to WAAM deposition direction.
- The best CFCG life enhancement in both materials was observed in vertical specimens, increasing the lifespan of ER70S-6 specimen by 45.8 % and ER100S-1 by 40.5 %.
- The effect of laser shock peening is pronounced while the crack is propagating through the treated area and can result in a deteriorating trend within the untreated region of the sample.
- Neutron and X-ray diffraction measurements revealed that LP introduces compressive residual stresses at the outer surface of the specimen within the treated area, which subsequently slows down the CFCG rates and prolongs the lifespan of the surface treated specimens.

CRediT authorship contribution statement

Anna Ermakova: Methodology, Validation, Formal analysis, Writing – original draft. **Jarryd Braithwaite:** Resources, Validation, Writing – review & editing. **Javad Razavi:** Conceptualization, Validation, Writing – review & editing. **Supriyo Ganguly:** Resources, Writing – review & editing. **Filippo Berto:** Conceptualization, Writing – review & editing. **Ali Mehmanparast:** Conceptualization, Resources, Writing – review & editing, Supervision.

Declaration of competing interest

The authors declare that they have no known competing financial interests or personal relationships that could have appeared to influence the work reported in this paper.

Data availability

Data will be made available on request.

Acknowledgements

This work was supported by grant EP/L016303/1 for Cranfield, Oxford, and Strathclyde Universities Centre for Doctoral Training in Renewable Energy Marine Structures – REMS CDT (http://www.rems-cdt.ac.uk/) from the UK Engineering and Physical Sciences Research Council (EPSRC). The authors would like to thank ILL-France for provision of the neutron beamtime for residual stress measurements under https://doi.ill.fr/10.5291/ILL-DATA.1-02-292 and ANSTO (Proposal 13422).

References

[1] O. Adedipe, F. Brennan, A. Kolios, Review of corrosion fatigue in offshore structures: present status and challenges in the offshore wind sector, Renew. Sust. Energ. Rev. 61 (2016) 141–154.
[2] G. Ersdal, J.V. Sharp, A. Stacey, Ageing and life extension of offshore structures: the challenge of managing structural integrity. https://books.google.no/books?id=tzB6DwAAQBAJ&pg=PA162&lpg=PA162&dq=grinding+life+extension+steels&source=bl&ots=mi7WNDonqm&sig=ACfU3U0IKLdC3UtdrW3JZXUPNkCiFC2eLQ&hl=en&sa=X&ved=2ahUKEwi4mpzh6sf3AhWuS_EDHTA-BQ4Q6AF6BAgPEAM#v=onepage&q=grindinglifeextens. (Accessed 5 May 2022).
[3] K.H. Kloos, B. Fuchsbauer, J. Adelmann, Fatigue properties of specimens similar to components deep rolled under optimized conditions, Int. J. Fatigue 9 (1987) 35–42.
[4] I. Altenberger, R.K. Nalla, Y. Sano, L. Wagner, R.O. Ritchie, On the effect of deep-rolling and laser-peening on the stress-controlled low- and high-cycle fatigue behavior of Ti–6Al–4V at elevated temperatures up to 550 °C, Int. J. Fatigue 44 (2012) 292–302.
[5] C.C. Wong, A. Hartawan, W.K. Teo, Deep cold rolling of features on aero-engine components, Procedia CIRP 13 (2014) 350–354.
[6] R.K. Nalla, I. Altenberger, U. Noster, G.Y. Liu, B. Scholtes, R.O. Ritchie, On the influence of mechanical surface treatments—deep rolling and laser shock peening—on the fatigue behavior of Ti–6Al–4V at ambient and elevated temperatures, Mater. Sci. Eng. A 355 (2003) 216–230.
[7] N. Tsuji, S. Tanaka, T. Takasugi, Effect of combined plasma-carburizing and deep-rolling on notch fatigue property of ti-6Al-4V alloy, Mater. Sci. Eng. A 499 (2009) 482–488.
[8] H. Luong, M.R. Hill, The effects of laser peening and shot peening on high cycle fatigue in 7050–T7451 aluminum alloy, Mater. Sci. Eng. A 527 (2010) 699–707.
[9] A.K. Gujba, M. Medraj, Laser peening process and its impact on materials properties in comparison with shot peening and ultrasonic impact peening, Mater 7 (2014) 7925–7974, 7, 7925–7974 (2014).
[10] Y.K. Gao, X.R. Wu, Experimental investigation and fatigue life prediction for 7475–T7351 aluminum alloy with and without shot peening-induced residual stresses, Acta Mater. 59 (2011) 3737–3747.
[11] P. Zhang, J. Lindemann, Influence of shot peening on high cycle fatigue properties of the high-strength wrought magnesium alloy AZ80, Scr. Mater. 52 (2005) 485–490.
[12] Z. Wang, C. Jiang, X. Gan, Y. Chen, V. Ji, Influence of shot peening on the fatigue life of laser hardened 17–4PH steel, Int. J. Fatigue 33 (2011) 549–556.
[13] O. Hatamleh, J. Lyons, R. Forman, Laser and shot peening effects on fatigue crack growth in friction stir welded 7075–T7351 aluminum alloy joints, Int. J. Fatigue 29 (2007) 421–434.
[14] O. Hatamleh, A comprehensive investigation on the effects of laser and shot peening on fatigue crack growth in friction stir welded AA 2195 joints, Int. J. Fatigue 31 (2009) 974–988.
[15] P. Ganesh, R. Sundar, H. Kumar, R. Kaul, K. Ranganathan, P. Hedaoo, P. Tiwari, L. M. Kukreja, S.M. Oak, S. Dasari, G. Raghavendra, Studies on laser peening of spring steel for automotive applications, Opt. Lasers Eng. 50 (2012) 678–686.
[16] G. Feldmann, C.C. Wong, W. Wei, T. Haubold, Application of vibropeening on aero – engine component, Procedia CIRP 13 (2014) 423–428.
[17] T.A. Rodrigues, V. Duarte, R.M. Miranda, T.G. Santos, J.P. Oliveira, Current status and perspectives on wire and arc additive manufacturing (WAAM), Mater 12 (2019) 1121, 12, 1121 (2019).
[18] C.R. Cunningham, J.M. Flynn, A. Shokrani, V. Dhokia, S.T. Newman, Invited review article: strategies and processes for high quality wire arc additive manufacturing, Addit. Manuf. 22 (2018) 672–686.
[19] P. Dong, in: Residual Stresses and Distortions in Welded Structures: A Perspective for Engineering Applications 10, 2013, pp. 389–398, https://doi.org/10.1179/174329305X29465.
[20] P. Dong, F.W. Brust, Welding residual stresses and effects on fracture in pressure vessel and piping components: a millennium review and beyond, J. Press. Vessel. Technol. 122 (2000) 329–338.
[21] G.A. Webster, A.N. Ezeilo, Residual stress distributions and their influence on fatigue lifetimes, Int. J. Fatigue 23 (2001) 375–383.
[22] M. Rauch, J. Hascoet, Improving Additive Manufactured Surfaces Properties With Post Processing Techniques, 2021.
[23] P.A. Colegrove, J. Donoghue, F. Martina, J. Gu, P. Prangnell, J. Hönnige, Application of bulk deformation methods for microstructural and material property improvement and residual stress and distortion control in additively manufactured components, Scr. Mater. 135 (2017) 111–118.
[24] F. Martina, M.J. Roy, B.A. Szost, S. Terzi, P.A. Colegrove, S.W. Williams, P. J. Withers, J. Meyer, M. Hofmann, in: Residual Stress of As-deposited and Rolled Wire+arc Additive Manufacturing Ti–6Al–4V Components 32, 2016, pp. 1439–1448, https://doi.org/10.1080/02670836.2016.1142704.
[25] J.R. Hönnige, P.A. Colegrove, S. Ganguly, E. Eimer, S. Kabra, S. Williams, Control of residual stress and distortion in aluminium wire + arc additive manufacture with rolling, Addit. Manuf. 22 (2018) 775–783.
[26] P.A. Colegrove, H.E. Coules, J. Fairman, F. Martina, T. Kashoob, H. Mamash, L. D. Cozzolino, Microstructure and residual stress improvement in wire and arc additively manufactured parts through high-pressure rolling, J. Mater. Process. Technol. 213 (2013) 1782–1791.
[27] A. Saboori, G. Piscopo, M. Lai, A. Salmi, S. Biamino, An investigation on the effect of deposition pattern on the microstructure, mechanical properties and residual

stress of 316L produced by directed energy deposition, Mater. Sci. Eng. A 780 (2020).
[28] M. Munther, T. Martin, A. Tajyar, L. Hackel, A. Beheshti, K. Davami, Laser shock peening and its effects on microstructure and properties of additively manufactured metal alloys: a review, Eng. Res. Express 2 (2020).
[29] R. Sun, L. Li, Y. Zhu, W. Guo, P. Peng, B. Cong, J. Sun, Z. Che, B. Li, C. Guo, L. Liu, Microstructure, residual stress and tensile properties control of wire-arc additive manufactured 2319 aluminum alloy with laser shock peening, J. Alloys Compd. 747 (2018) 255–265.
[30] S. Luo, W. He, K. Chen, X. Nie, L. Zhou, Y. Li, Regain the fatigue strength of laser additive manufactured ti alloy via laser shock peening, J. Alloys Compd. 750 (2018) 626–635.
[31] J. Chi, Z. Cai, Z. Wan, H. Zhang, Z. Chen, L. Li, Y. Li, P. Peng, W. Guo, Effects of heat treatment combined with laser shock peening on wire and arc additive manufactured Ti17 titanium alloy: microstructures, residual stress and mechanical properties, Surf. Coat. Technol. 396 (2020), 125908.
[32] M. Manikandan, S.S. Mani Prabu, S. Jayachandran, K. Akash, I.A. Palani, K. P. Karunakaran, in: Influence of Laser Shock Peening on Wire Arc Additive Manufactured Low Carbon Steel, 2019, pp. 509–516, https://doi.org/10.1007/978-981-32-9425-7_45.
[33] C. Wang, K. Luo, X. Bu, Y. Su, J. Cai, Q. Zhang, J. Lu, Laser shock peening-induced surface gradient stress distribution and extension mechanism in corrosion fatigue life of AISI 420 stainless steel, Corros. Sci. 177 (2020), 109027.
[34] Lincoln Electric Company, T. Lincoln ® ER70S-6 Welding Positions Typical Applications.
[35] ER100S-G Data Sheet, Bohler Welding, 2014.
[36] A. Ermakova, A. Mehmanparast, S. Ganguly, A review of present status and challenges of using additive manufacturing technology for offshore wind applications, Procedia Struct. Integr. 17 (2019) 29–36.
[37] ASTM E647−13, Standard test method for measurement of fatigue crack growth rates, Am. Soc. Test. Mater. (2014) 1–50, https://doi.org/10.1520/E0647-15E01.2.
[38] American Society for Testing and Materials, ASTME-1820-11: standard test method for measurement of fracture toughness, Annu. B. ASTM Stand. 1–55 (2011), https://doi.org/10.1520/E1820-18.
[39] D. Pi, A. Ermakova, A. Mehmanparast, Numerical analysis of surface rolling effects on fatigue life enhancement of wire arc additively manufactured parts, J. Multiscale Model. 2146001 (2022) 1–16.
[40] A.collab International, D1141-98 standard practice for the preparation of substitute ocean water, ASTM Int. 98 (2013) 1–3.
[41] A. Mehmanparast, F. Brennan, I. Tavares, Fatigue crack growth rates for offshore wind monopile weldments in air and seawater: SLIC inter-laboratory test results, Mater. Des. 114 (2017) 494–504.
[42] A. Henderson, Hydrodynamic Loading of Offshore Wind Turbines, 2003.
[43] A. Jacob, A. Mehmanparast, R. D'Urzo, J. Kelleher, Experimental and numerical investigation of residual stress effects on fatigue crack growth behaviour of S355 steel weldments, Int. J. Fatigue 128 (2019), 105196.
[44] O. Adedipe, F. Brennan, A. Kolios, Corrosion fatigue load frequency sensitivity analysis, Mar. Struct. 42 (2015) 115–136.
[45] J.C. Newman, Y. Yamada, M.A. James, Back-face strain compliance relation for compact specimens for wide range in crack lengths, Eng. Fract. Mech. 78 (2011) 2707–2711.
[46] C.Y. Hou, Fatigue analysis of welded joints with the aid of real three-dimensional weld toe geometry, Int. J. Fatigue 29 (2007) 772–785.
[47] A. Ermakova, J. Razavi, S. Cabeza, E. Gadalinska, M. Reid, A. Paradowska, S. Ganguly, F. Berto, A. Mehmanparast, The influence of wire arc additive manufacturing deposition process on residual stress distribution and fatigue life in the presence and absence of surface treatment, Addit. Manuf. (2022). - submitted manuscript.
[48] A. Ermakova, S. Ganguly, J. Razavi, F. Berto, A. Mehmanparast, Corrosion-fatigue crack growth behaviour of wire arc additively manufactured ER70S-6 steel parts in marine environments, Eur. J. Mech. A/Solids 96 (2022), 104739.
[49] A. Ermakova, S. Ganguly, J. Razavi, F. Berto, A. Mehmanparast, Corrosion-fatigue crack growth behaviour of wire arc additively manufactured ER100S-1 steel specimens, Eng. Fail. Anal. 138 (2022), 106362.
[50] T. Pirling, G. Bruno, P.J. Withers, SALSA—a new instrument for strain imaging in engineering materials and components, Mater. Sci. Eng. A 437 (2006) 139–144.
[51] R. Pynn, L. Liang, in: Neutron Scattering—A Non-destructive Microscope for Seeing Inside Matter, 2009, pp. 15–36, https://doi.org/10.1007/978-0-387-09416-8_2.
[52] M.T. Hutchings, P.J. Withers, T.M. Holden, T. Lorentzen, Introduction to the Characterization of Residual Stress by Neutron Diffraction. Introd. to Charact. Residual Stress by Neutron Diffr, 2005, https://doi.org/10.1201/9780203402818.
[53] Z. Barsoum, I. Barsoum, Residual stress effects on fatigue life of welded structures using LEFM, Eng. Fail. Anal. 16 (2009) 449–467.